

## Article

# Lateral Heat Distribution Characteristics of CLP S275 Using Gaussian FFT Algorithm in Optical Thermographic Testing

Seungju Lee <sup>1</sup>, Yoonjae Chung <sup>1</sup>, Wontae Kim <sup>1,\*</sup> and Hyunkyu Suh <sup>2,\*</sup>

<sup>1</sup> Eco-Sustainable Energy Research Institute, Kongju National University, 1223-24 Cheonan-daero, Seobuk-gu, Cheonan-si 31080, Republic of Korea; cow123456798@smail.kongju.ac.kr (S.L.); dbswosla79@kongju.ac.kr (Y.C.)

<sup>2</sup> Division of Mechanical and Automotive Engineering, Kongju National University, 1223-24 Cheonan-daero, Seobuk-gu, Cheonan-si 31080, Republic of Korea

\* Correspondence: kwt@kongju.ac.kr (W.K.); hksuh@kongju.ac.kr (H.S.); Tel.: +82-41-521-9380 (W.K.); +82-41-521-9264 (H.S.)

**Abstract:** In general, when using infrared thermography (IRT) techniques to excite a heat source on the surface of an inspection object, the heat source is focused on the center of the image of the infrared (IR) camera. If the object to be inspected is small, uniform excitation of the heat source is possible, but if the area is large, the heat source is concentrated locally, resulting in uneven heat distribution. Therefore, in this study, heat distribution was analyzed after inducing a non-uniform heat source by exciting the heat source at different locations. Additionally, the fast Fourier transform (FFT) algorithm with Gaussian filtering was applied to resolve the non-uniform distribution of the heat sources. Excellent results were obtained from the amplitude image, and the effectiveness of the FFT algorithm was verified using the Otsu algorithm. Finally, the signal-to-noise ratio (SNR) was calculated, and the detection ability according to each thinning rate was analyzed.

**Keywords:** optical thermography; fast Fourier transform; Gaussian filtering; thermal equalization; validation evaluation



**Citation:** Lee, S.; Chung, Y.; Kim, W.; Suh, H. Lateral Heat Distribution Characteristics of CLP S275 Using Gaussian FFT Algorithm in Optical Thermographic Testing. *Appl. Sci.* **2024**, *14*, 3776. <https://doi.org/10.3390/app14093776>

Academic Editor: Giuseppe Lacidogno

Received: 1 April 2024  
Revised: 26 April 2024  
Accepted: 26 April 2024  
Published: 28 April 2024



**Copyright:** © 2024 by the authors. Licensee MDPI, Basel, Switzerland. This article is an open access article distributed under the terms and conditions of the Creative Commons Attribution (CC BY) license (<https://creativecommons.org/licenses/by/4.0/>).

## 1. Introduction

As the importance of energy is in the spotlight in modern society, dependence on ESG is gradually decreasing. As a result, the importance of nuclear energy is receiving attention again around the world. However, most nuclear power plants have been in use for at least several decades, and cases of corrosion of the containment liner plate (CLP) [1–3], which plays a role in protecting nuclear energy, are gradually increasing. If corrosion occurs in the CLP, it progresses to a thinning defect. If maintenance is not carried out properly and thinning continues, it will eventually lead to breakage and cause significant damage [4]. For this reason, real-time maintenance of the CLP is essential. However, the efficiency is very low if a person needs to inspect the surface directly because the area is very large. Therefore, testing is being conducted using non-destructive testing (NDT) techniques [5,6].

Among the NDT techniques, ultrasonic testing (UT) and echo impact (EI) techniques are the most widely used. The UT technique has the advantage of accurately measuring the thickness of a plate by contact with an ultrasonic probe, but has the disadvantage of consuming a significant amount of time when a large area is being inspected because it requires a contact point [7,8]. The EI technique can identify resonance frequencies in the frequency domain of the vibration signals acquired using the fast Fourier transform (FFT), and, through this, information about voids in concrete can be acquired [9–11]. However, since it hits a random area, it is difficult to obtain quantitative data. Additionally, there is little response in heavily damped masonry bridges. Therefore, the active infrared thermography (IRT) technique, which allows the inspection of large areas in real time, has recently been in the spotlight.

The active IRT technique is a technique that uses an external heat source to provide heat to the inspection object and then detects the emitted radiant energy with an infrared (IR) camera [12,13]. External heat sources such as optical, electromagnetic, vibration, and microwave can be selected appropriately depending on the inspection object and surrounding environment. The area of the CLP of nuclear power plants in Korea is generally too large, and the UT technique, which is used most widely in Korea, has very high accuracy, but it takes at least two months to inspect even one power plant. Therefore, in this study, thinning defect evaluation was performed using a halogen lamp, one of the optical techniques.

In recent years, IRT technology has made great progress by applying artificial intelligence (AI). Liu et al. proposed a deep convolutional autoencoder thermography (DCAT) data analysis technique [14]. The original data were restored using the proposed technique to reduce noise and uneven background. In addition, by using a deep autoencoder, non-linear features can be extracted to obtain information about the internal structure and defects of a modern artwork that is the object of inspection. Akhloufi et al. proposed a technique that converts the 2D images acquired using IRT techniques into 3D images, enabling the visualization of defects that exist inside the inspection object and providing location information on the actual defects [15]. Liu et al. proposed a deep autoencoder thermography (DAT) technique to detect surface defects in composite materials [16]. Information can be acquired from the non-linear temperature profile of the multi-layer structure, and defect information is provided by visualizing hidden layers.

When inspecting an object with a large surface area, such as a CLP, using a halogen lamp [17], the inspection is performed without knowing the location of the internal defect. In this case, the heat is provided intensively from the surface due to the lamp, rising locally. If relatively little heat is generated at the location of the internal defect, detectability is affected. Therefore, to solve this problem, this study presents a thermal equalization process by applying Gaussian filtering to the FFT algorithm.

Generally, when a halogen lamp is used, the heat source is excited in the form of a sine wave, and phase and amplitude data are acquired using the four-point algorithm of the lock-in thermography (LIT) technique. However, when a non-uniform heat source is provided, the detectability of the phase and amplitude data is reduced, thereby reducing reliability. Therefore, in this study, phase and amplitude data were acquired after applying thermal equalization to the raw image using the FFT algorithm. The process of performing thermal equalization was conducted by applying the Gaussian filtering-based FFT algorithm to thermal images acquired through two types of heat sources. Here, the two types of heat sources are long pulse and sine waveform.

Afterwards, to evaluate the effect of heat homogenization using the FFT algorithm, a qualitative evaluation using the Otsu algorithm and a quantitative evaluation calculating the signal-to-noise ratio (SNR) were performed. The signal-to-noise ratio (SNR) of the defective area was evaluated with and without the FFT algorithm to evaluate its effectiveness.

The structure of this study is as follows. In Section 2, a formula combining the FFT algorithm and Gaussian filtering and the theory of the LIT technique are presented. Section 3 presents two types of test specimens made of S275 material depicting a CLP and the performance of the LIT test equipment. In addition, the three positions of the heat source that provide a non-uniform heat source are explained. Section 4 analyzes the results of the thermal equalization when the FFT algorithm was applied to the raw image, phase image, and amplitude image, and the SNR technique and Otsu algorithm is evaluated to verify its effectiveness. Section 5 presents the conclusion of this study.

## 2. Theory

### 2.1. FFT-Based Gaussian Filtering

Gaussian filtering is used to remove high-frequency noise from images and create a smooth effect. Through this, the effect can be achieved of reducing the sharpness of the image and reducing noise. However, it has the disadvantage of blurring clear edges

within the image. By combining this with the FFT algorithm, frequency components can be analyzed more clearly, noise can be removed, and quantitative data can be acquired in local feature areas. Gaussian filtering is defined in the spatial domain and mainly utilizes 2D Gaussian filtering [18].

$$H(x, y) = e^{-\frac{x^2+y^2}{2\sigma^2}} \tag{1}$$

where  $x$  and  $y$  are coordinates in the spatial domain and  $\sigma$  means standard deviation of the Gaussian filtering. Afterwards, the image and the Gaussian filtering are combined.

$$g(x, y) = f(x, y) \cdot H(x, y) \tag{2}$$

where  $f(x, y)$  means the input image and  $H(x, y)$  means the Gaussian filtering. Afterwards, the FFT is applied to the synthesized image.

$$G(u, v) = \text{FFT}\{g(x, y)\} \tag{3}$$

where  $G(u, v)$  means the image in frequency domain. Afterwards, the image is acquired by applying the Gaussian filtering in the frequency domain.

$$\hat{F}(u, v) = G(u, v) \cdot H(u, v) \tag{4}$$

where  $\hat{F}(u, v)$  means the image in frequency domain with the final Gaussian filtering applied. Afterwards, the inverse FFT (IFFT) is applied to convert the frequency domain image with the Gaussian filtering applied to the spatial domain.

$$\hat{f}(x, y) = \text{IFFT}\{\hat{F}(u, v)\} \tag{5}$$

where  $\hat{f}(x, y)$  means the final Gaussian filtered image.

Figure 1 shows the process of removing noise and performing thermal equalization using Gaussian filtering. The weighted average is calculated by applying a kernel to each pixel of the image, and the larger the kernel size, the greater the influence on the surrounding pixels. This removes noise by replacing values around noisy pixels with smooth values. At the same time, the FFT algorithm is applied to convert to the frequency domain and then process the non-uniform heat source.

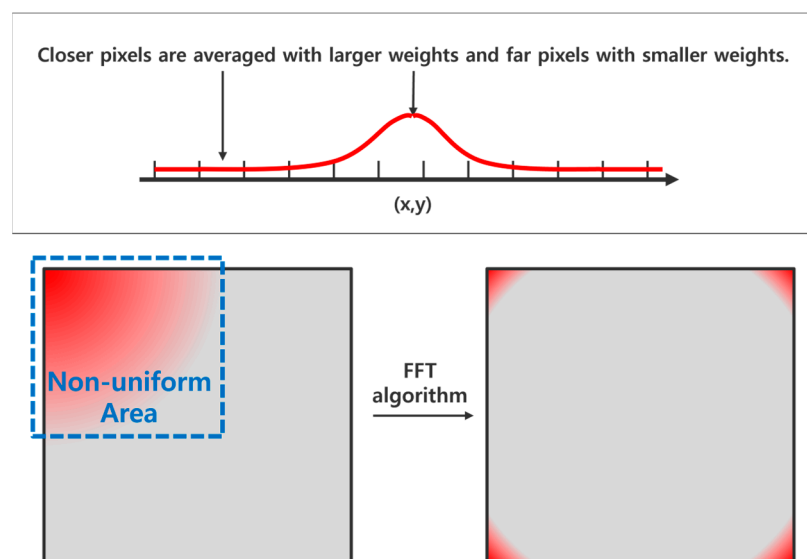


Figure 1. The principle of Gaussian filtering-based FFT algorithm.

## 2.2. Lock-in Thermography

LIT is a technique that measures the radiant energy that reacts from an inspection object when a sinusoidal heat source is excited on the inspection object [19–21]. Afterwards, the phase and amplitude data of infrared energy are extracted using the four-point algorithm. Temperature mapping is performed based on the extracted data to generate a temperature distribution map for the surface of the object. The temperature distribution obtained in this way expresses the temperature change occurring on the surface at high resolution. The equation for acquiring phase and amplitude images is as follows [22]:

$$\phi = \tan^{-1} \left( \frac{S_1 - S_3}{S_2 - S_4} \right) \quad (6)$$

$$A = \sqrt{(S_1 - S_3)^2 + (S_2 - S_4)^2} \quad (7)$$

where  $\phi$  is the phase and  $A$  is the amplitude.  $S_1$ ,  $S_2$ ,  $S_3$ , and  $S_4$  are four images at constant intervals. After applying the Gaussian filtering-based FFT algorithm to  $S_1$ ,  $S_2$ ,  $S_3$ , and  $S_4$ , the phase and amplitude data were acquired. Afterwards, the detectability of the defective area and sound area was evaluated according to the Gaussian weights.

## 3. Experimental Setup

### 3.1. Experimental Devices

In this study, one halogen lamp was used at set positions in three areas and then excited with a sinusoidal heat source for one cycle. The output of the halogen lamp was 1 kW and the lamp was placed perpendicular to the S275 specimen. The frequency is controlled by a function generator, and it was set to 0.01 Hz. Additionally, the power amplifier can control the output and it was set to 10 V. The IR camera was FLIR's SC645 (Teledyne FLIR, Wilsonville, OR, USA) (un-cooled,  $640 \times 480$  pixels, 7.5–13  $\mu\text{m}$ , 50 Hz) model, and the frame rate was set to 50 Hz. The distance from the S275 specimen was 500 mm. The IR camera and halogen lamp were placed in the same location. Figure 2 shows the experimental setup of this study.

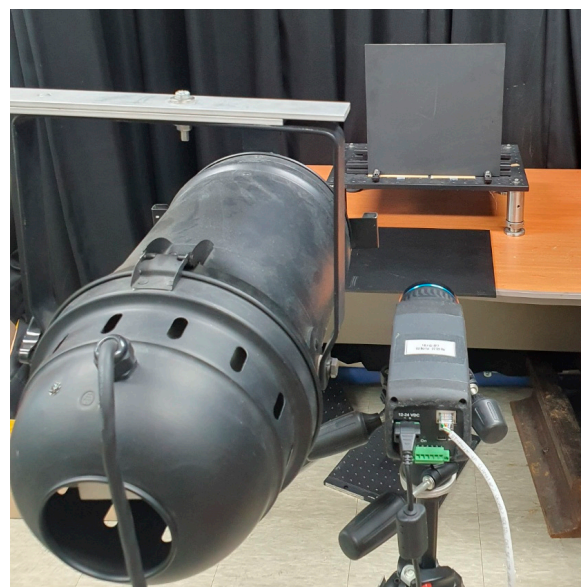


**Figure 2.** Configuration of LIT experimental devices.

### 3.2. S275 Specimen

In this study, two types of S275 specimens were used, and Figure 3 shows the shape of the S275 specimens. The A-type specimen is flattened with no defects, and the B-type

specimen has 9 thinning defects and is 6 mm thick. In B-type specimen, the thinning rate was produced regularly from 10 to 90%, and the size was the same at  $40 \times 40$  mm. Figure 4 shows the dimensions of the A- and B-type specimens. KRYLON’s black paint (KRYLON Inc., Norristown, PA, USA) was applied to both of the S275 specimens to maintain an emissivity above 0.95.

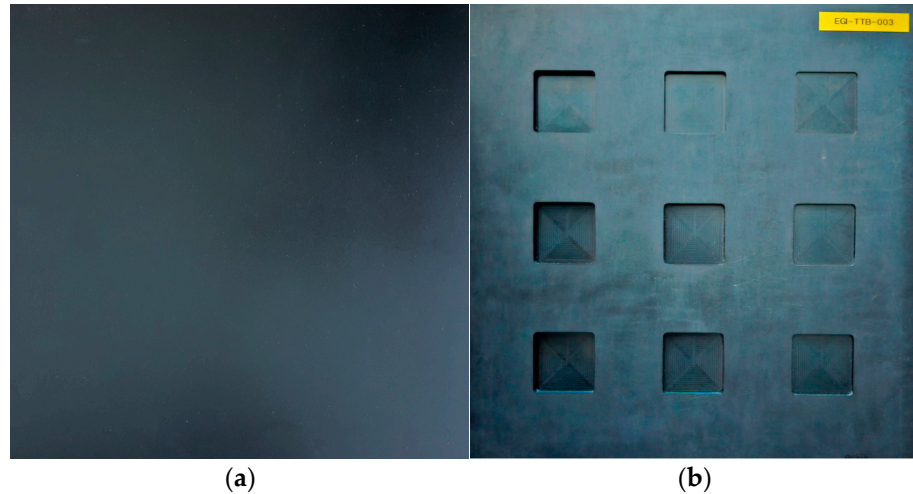


**Figure 3.** Two types of S275 specimen shapes. The A-type specimen has a flat surface without defects, and the B-type specimen has 9 artificial defects. (a) A-type specimen; (b) B-type specimen.

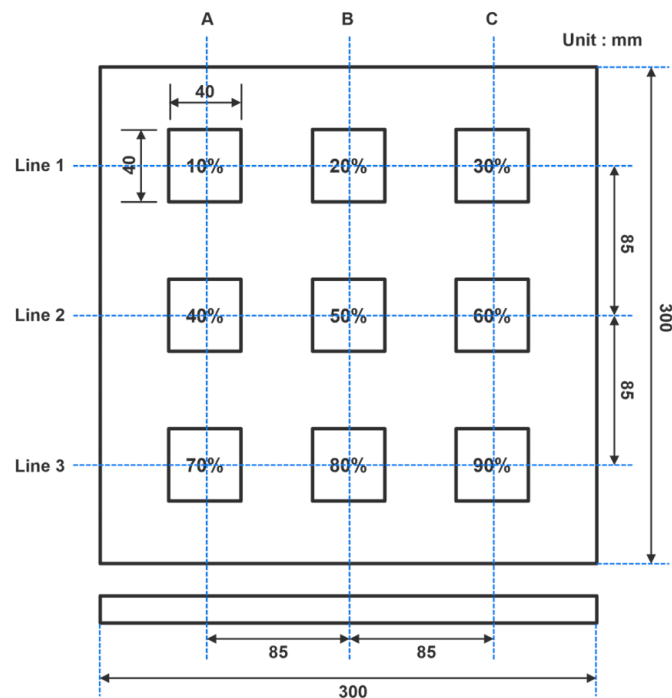


**Figure 4.** Dimensions of S275 specimen with 9 artificial thinning defects.

### 3.3. Position and Wave Form of Thermal Source Excitation

In this study, halogen lamps were not placed only in the center of the specimen, as in previous studies, but were also placed at the sides to induce uneven heat distribution. In actual industrial sites, uniform heat distribution cannot generally be expected when inspecting a large-area structure. Therefore, three positions were selected to demonstrate thermal equalization when a heat source was excited at a random location. Figure 5 shows the locations of the three positions.

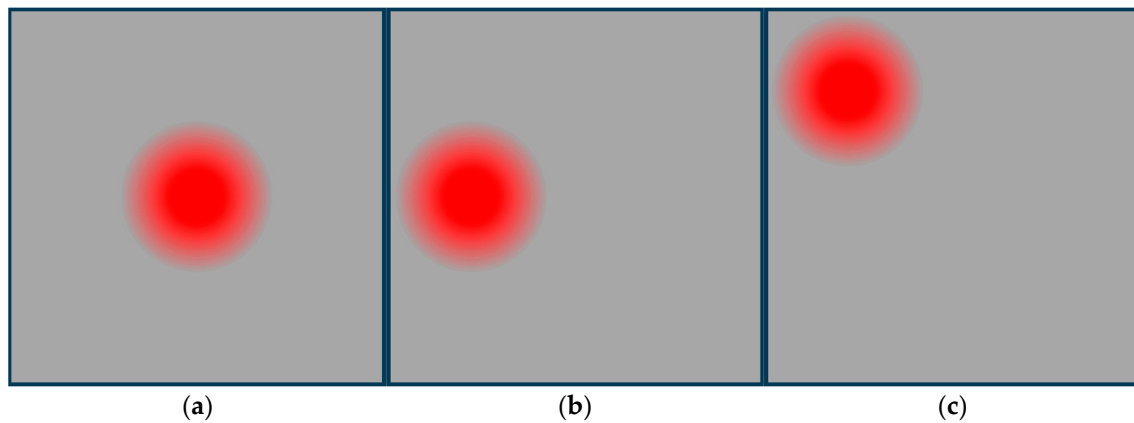


**Figure 5.** Three arrangements of halogen lamps to excite non-uniform heat sources. (a) center; (b) left side; (c) top left.

The type of heat source was divided into two types and classified into two types of experiments. The first is a long pulse type, and the thermal equalization was evaluated by applying the FFT algorithm to the thermal image. The second is a sine waveform, and the thermal equalization was evaluated by applying the FFT algorithm to four images with application of the four-point algorithm and then acquiring phase and amplitude images. The excitation frequency of the sine wave was set to 0.01 Hz and applied to each location. Figure 6 shows the two types of heat sources. After acquiring the temperature distribution images by applying the two types of heat sources, the phase and amplitude images were acquired to apply the FFT algorithm to thermal equalization.

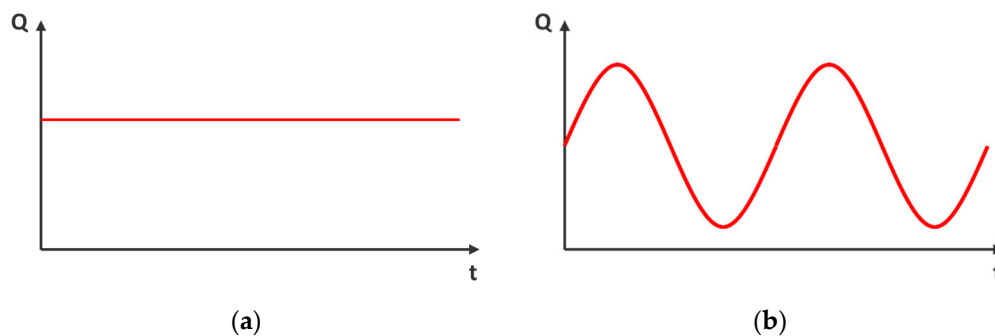


**Figure 6.** Thermal wave form of raw (temperature distribution) and lock-in algorithm. (a) Long pulse; (b) sine wave.

## 4. Results

### 4.1. Results of Applying FFT to Thermal Image

#### 4.1.1. Thermal Image of Long Pulse Wave

In this study, for the first time, the analysis of raw (temperature distribution) images was performed by exciting a long-pulse-type heat source. Figures 7 and 8 show the raw images of the A-type and type B specimens, and heat sources were provided at three positions. Figure 7 shows that there are no thinning defects, and the heat distribution occurs exactly at the location set by the inspector. In Figure 8a, only the thinning defects of C2 and C3 can be clearly detected, and in Figure 8b,c, clear detection is difficult due to the excitation of the non-uniform heat source. Afterwards, the thermal equalization process was performed by applying the FFT algorithm.

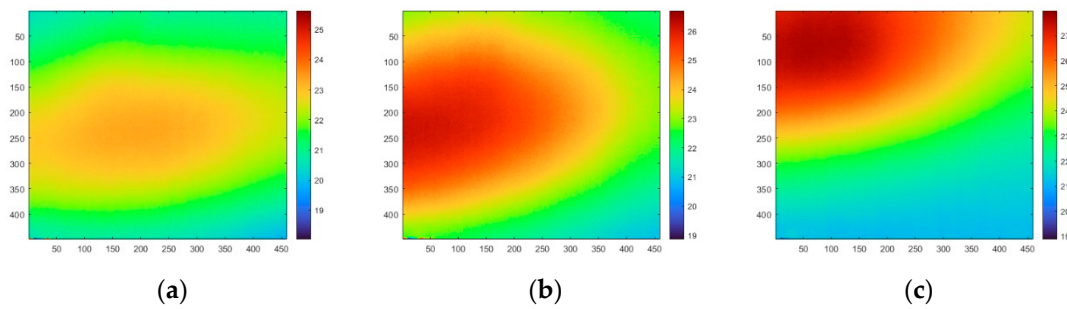


**Figure 7.** Thermal image of A-type specimen. (a) center; (b) left side; (c) top left.

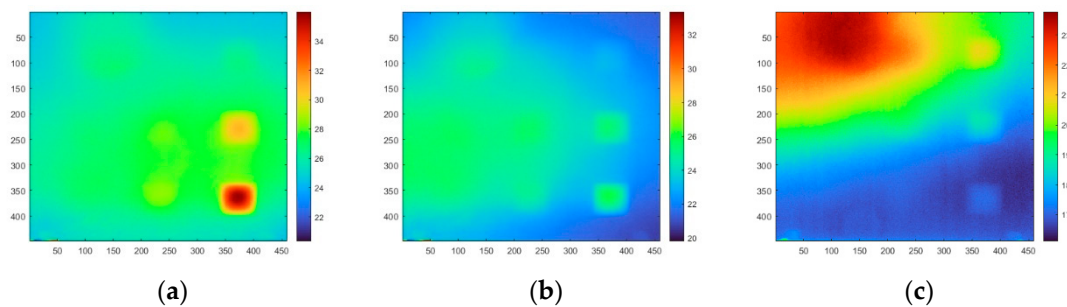


**Figure 8.** Thermal image of B-type specimen. (a) center; (b) left side; (c) top left.

#### 4.1.2. FFT Image of Long Pulse Wave

Figures 9 and 10 show images where the FFT algorithm was applied to the A- and B-type specimens after setting the Gaussian weight to 2.0. In Figure 9, after applying the FFT algorithm, thermal equalization is applied to confirm a uniform image. However, due to the low value of the Gaussian weight, high and low frequencies exist locally on the sides, as shown in Figure 9b,c. This can be solved by increasing the weight value, but the defective area is also relatively affected, causing the thinning defect to become unclear. In Figure 10, it can be seen that, although thermal equalization can be confirmed by applying the FFT algorithm, this does not significantly affect the detection of thinning defects. Therefore, the trends were quantitatively compared and analyzed through the Line 2 profile.

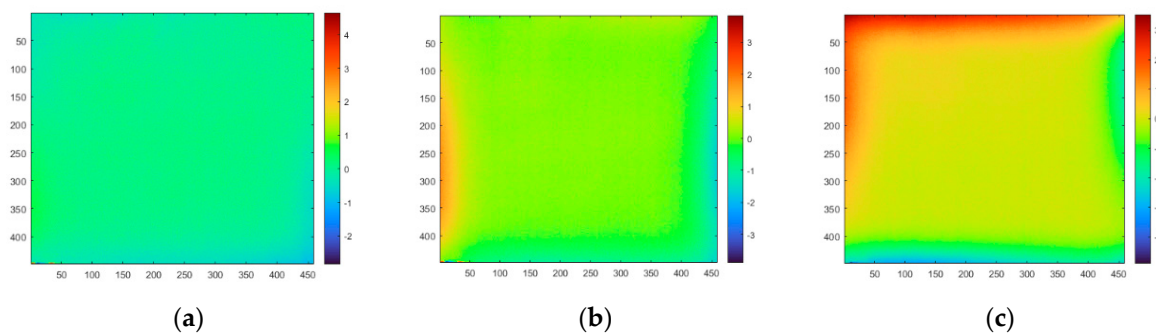


**Figure 9.** Gaussian-filtered image with FFT algorithm applied to type A specimen. Gaussian weights are set to 2.0. (a) center; (b) left side; (c) top left.

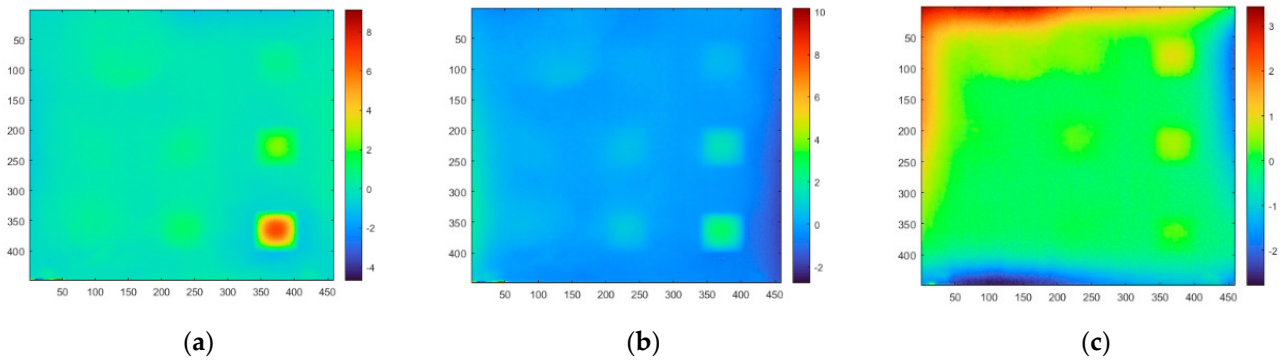


**Figure 10.** Gaussian-filtered image with FFT algorithm applied to type B specimen. Gaussian weights are set to 2.0. (a) center; (b) left side; (c) top left.

4.1.3. Thermal Equalization Trend Analysis of Long Pulse Wave

Figure 11 shows the Line 2 profile graph with the FFT algorithm applied to the images shown in Figures 9 and 10. In Figure 11, the higher the Gaussian weight of the raw image, the higher the influence of thermal equalization. In particular, as the weight increases from 0.5 to 4.0, as shown in Figure 11c, flattening is performed better in the center of the surface, making it possible to clearly detect C2 thinning defects in a uniform state, as shown in Figure 11f. When the FFT algorithm was applied to the raw image, a clear thermal equalization effect occurred when there were no defects. However, it can be confirmed that there is not much difference in detectability when a defect exists.

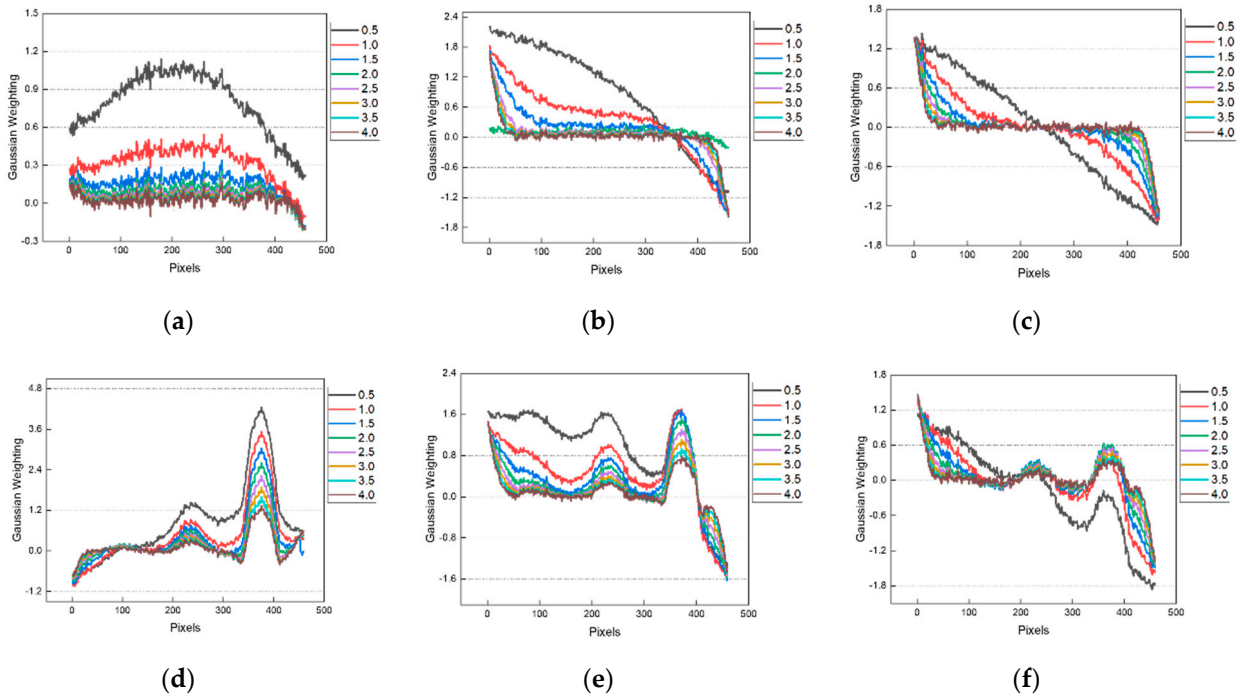


**Figure 11.** Profile graph of Line 2 with FFT applied for A- and B-type specimens. (a) A-type, center; (b) A-type, left side; (c) A-type, top left; (d) B-type, center; (e) B-type, left side; (f) B-type, top left.

4.2. Results of FFT Application to Phase Image

4.2.1. Phase Image of Sine Wave

Figures 12 and 13 show the phase images of the A- and B-type specimens acquired by the lock-in algorithm. Unlike the thermal image in Figure 12, the A-type specimen in Figure 12 does not show a qualitatively clear local phase distribution. In the phase image of

the B-type specimen in Figure 13, a clear Line C thinning defect can be detected. However, in Figure 13c, it can be seen that the result of the noise occurring in the lower right corner is due to the excitation of the non-uniform heat source. Therefore, thermal equalization was performed by applying the FFT algorithm.

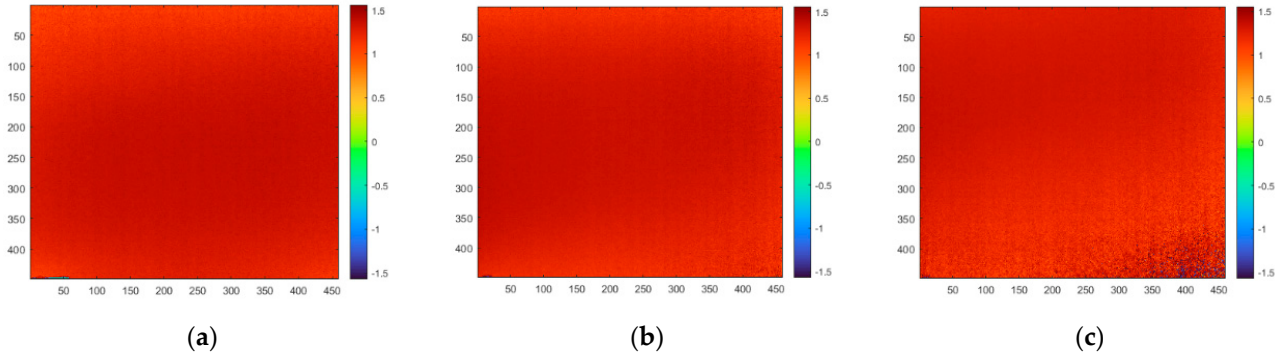


Figure 12. Phase image of A-type specimen. (a) center; (b) left side; (c) top left.

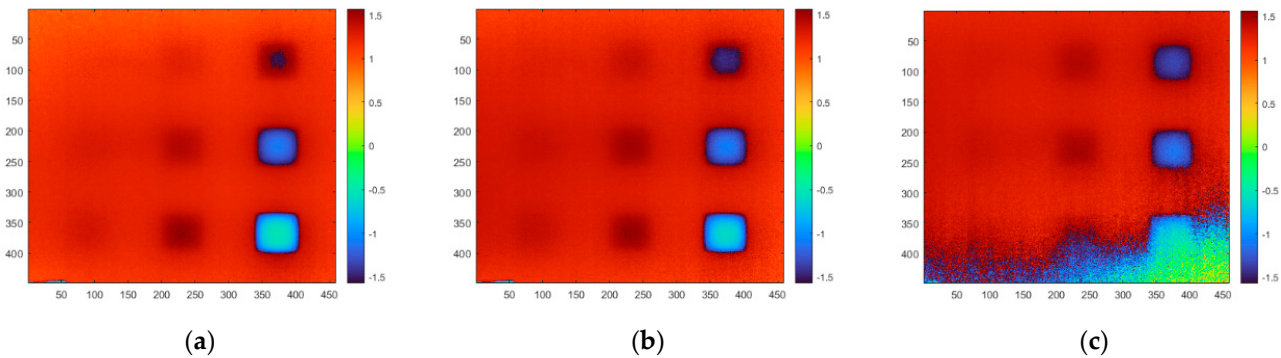


Figure 13. Phase image of B-type specimen. (a) center; (b) left side; (c) top left.

#### 4.2.2. Phase Image with FFT of Sine Wave

Figures 14 and 15 show phase images to which the FFT algorithm was applied to A- and B-type specimens after setting the Gaussian weight to 2.0. In Figure 14, it can be seen that, when applying the FFT, the higher the weight, the more the low frequencies are concentrated in the center, generating noise. As a result, noise exists around the defective area, as shown in Figure 15, and the higher the Gaussian weight, the more noise patterns occur in the sound area. However, compared to Figure 13, many thinning defects can be visually detected. For the quantitative analysis, the trends were quantitatively compared and analyzed through the Line 2 profile.

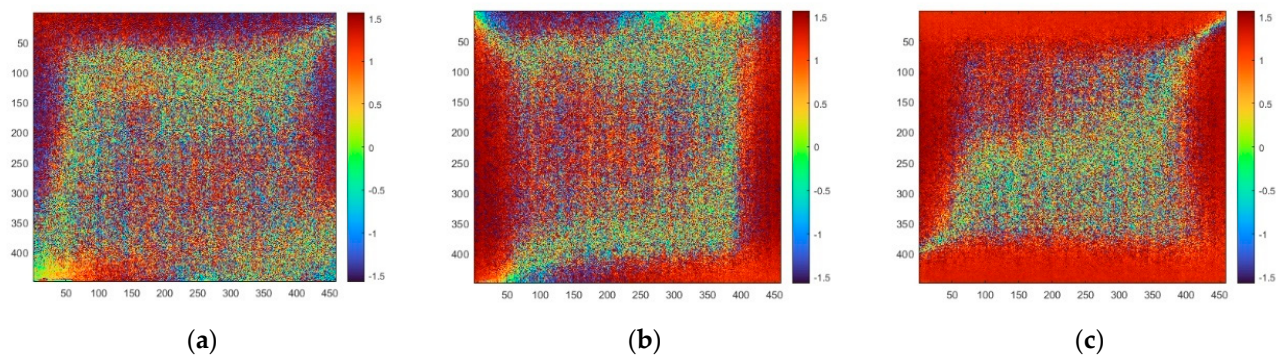
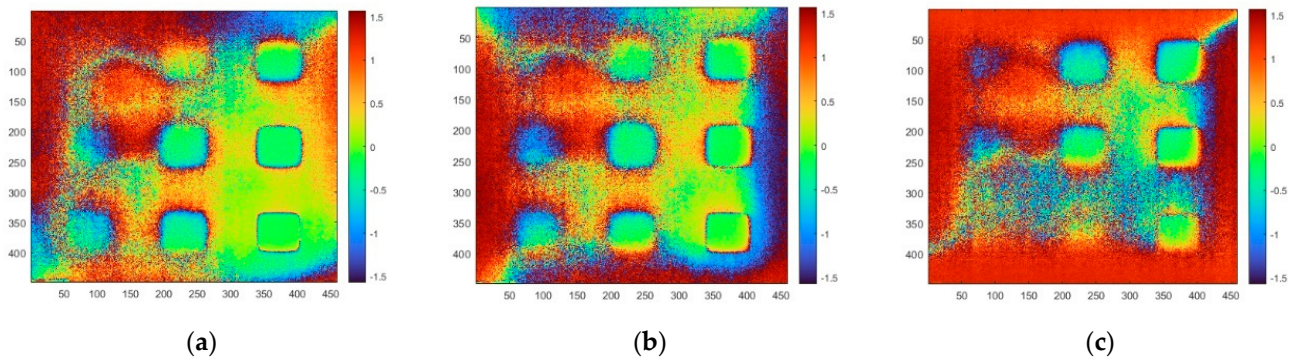


Figure 14. Phase image with FFT applied of A-type specimen. (a) center; (b) left side; (c) top left.



**Figure 15.** Phase image with FFT applied of B-type specimen. (a) center; (b) left side; (c) top left.

#### 4.2.3. Sine Wave Phase Thermal Equalization Trend Analysis

Figure 16 shows the Line 2 profile graph with the FFT algorithm applied to the phase image shown in Figure 15. In Figure 15, the boundary line of the defective area is converted to a high-frequency form, allowing relatively more thinning defects to be detected, which can be confirmed in the box outlined by the red dash in the graph. As the Gaussian weight increases, the thermal equalization is better applied, but more noise occurs around the defective area, making it difficult to clearly identify the boundary of the defective area. For the Line A thinning defects, it is difficult to identify the boundaries of the defective area due to the noise, regardless of the Gaussian weight. As a result, the number of defects detected in the phase image increased, but a lot of noise was generated, so the effectiveness of the FFT algorithm with the Gaussian filtering was judged to be reduced.

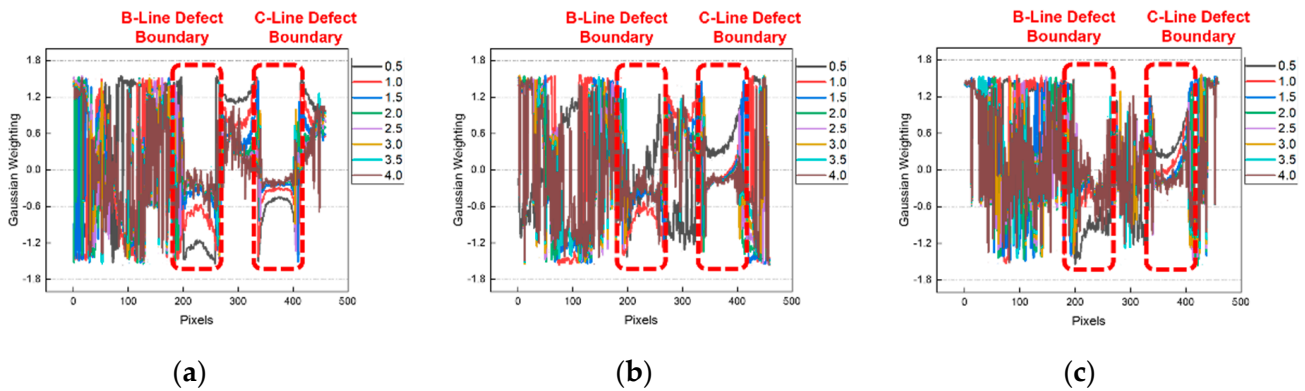


**Figure 16.** Line 2 phase profile graph using FFT for B-type specimen. (a) B-type, center; (b) B-type, left side; (c) B-type, top left.

### 4.3. Results of Applying FFT to Amplitude Image

#### 4.3.1. Amplitude Image of Sine Wave

Figures 17 and 18 show the amplitude images of the type A and B specimens acquired by the lock-in algorithm. In Figure 17, unlike in Figure 12, the location of the uneven heat source can be clearly identified. Figure 18 shows that there is difficulty in detecting the clear thinning defects due to the excitation of the non-uniform heat source. Therefore, the FFT algorithm was applied to improve the detectability.

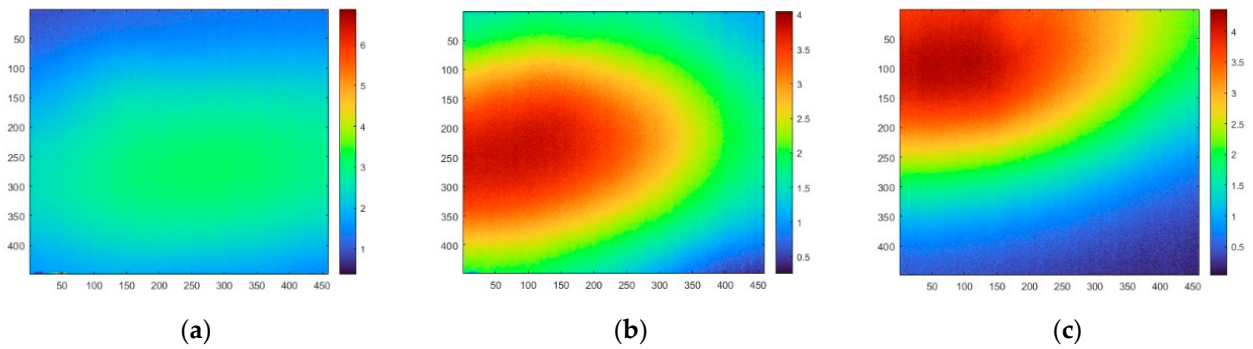


Figure 17. Amplitude images of A-type specimen. (a) center; (b) left side; (c) top left.

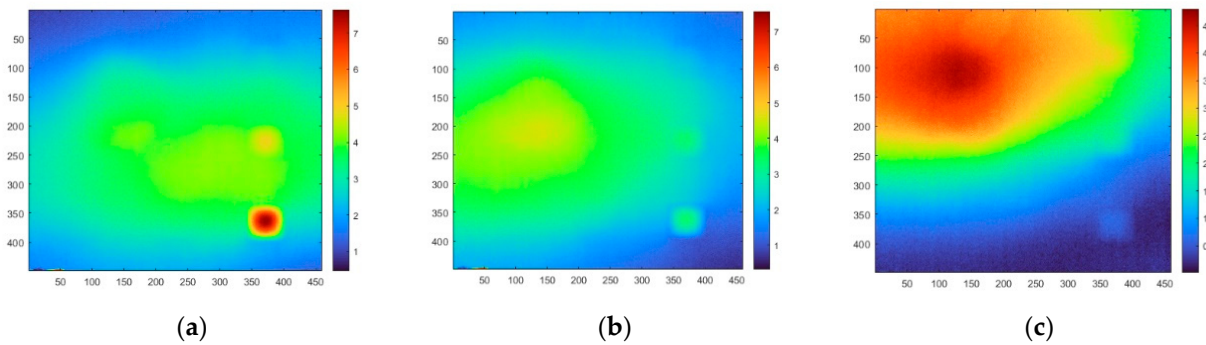


Figure 18. Amplitude images of B-type specimen. (a) center; (b) left side; (c) top left.

#### 4.3.2. Amplitude Image with FFT of Sine Wave

Figures 19 and 20 show the amplitude images in which the FFT algorithm was applied to the A- and B-type specimens after setting the Gaussian weight to 2.0. In Figure 19b,c, a pattern can be seen in which the high frequency was shifted to the side when the FFT algorithm was applied. Also, unlike in the phase image, relatively little noise occurred. Through this, it can be seen in Figure 20 that the detectability is greatly improved by applying the FFT algorithm. Improving the Gaussian weight can reduce the influence of high frequencies present on the side, but this also reduces the high-frequency data of the defect area, reducing detectability. Therefore, setting an appropriate Gaussian weight is required for optimal detectability.

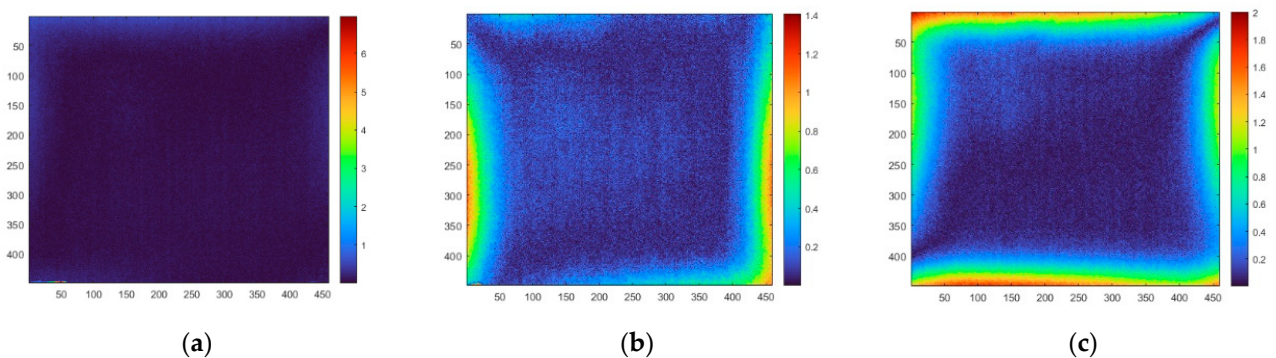


Figure 19. Amplitude image with FFT applied of A-type specimen. (a) center; (b) left side; (c) top left.

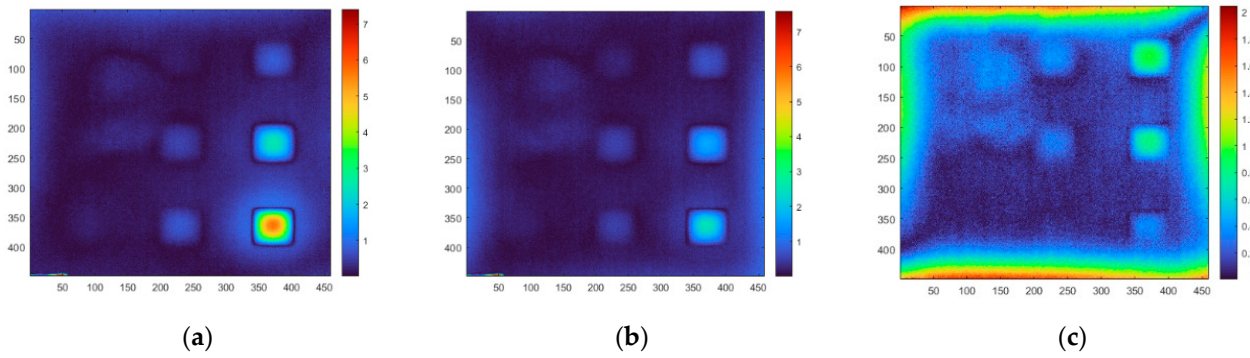


Figure 20. Amplitude image with FFT applied of B-type specimen. (a) center; (b) left side; (c) top left.

### 4.3.3. Amplitude Thermal Equalization Trend Analysis of Sine Wave

Figure 21 shows the Line 2 profile graph with the FFT algorithm applied to the amplitude image shown in Figure 20. In the case of the specimen Line A profile, it can be seen that the higher the Gaussian weight, the higher the effect of the thermal equalization. This makes it possible to clearly detect thinning defects when applying the FFT algorithm, as shown in Figure 21.

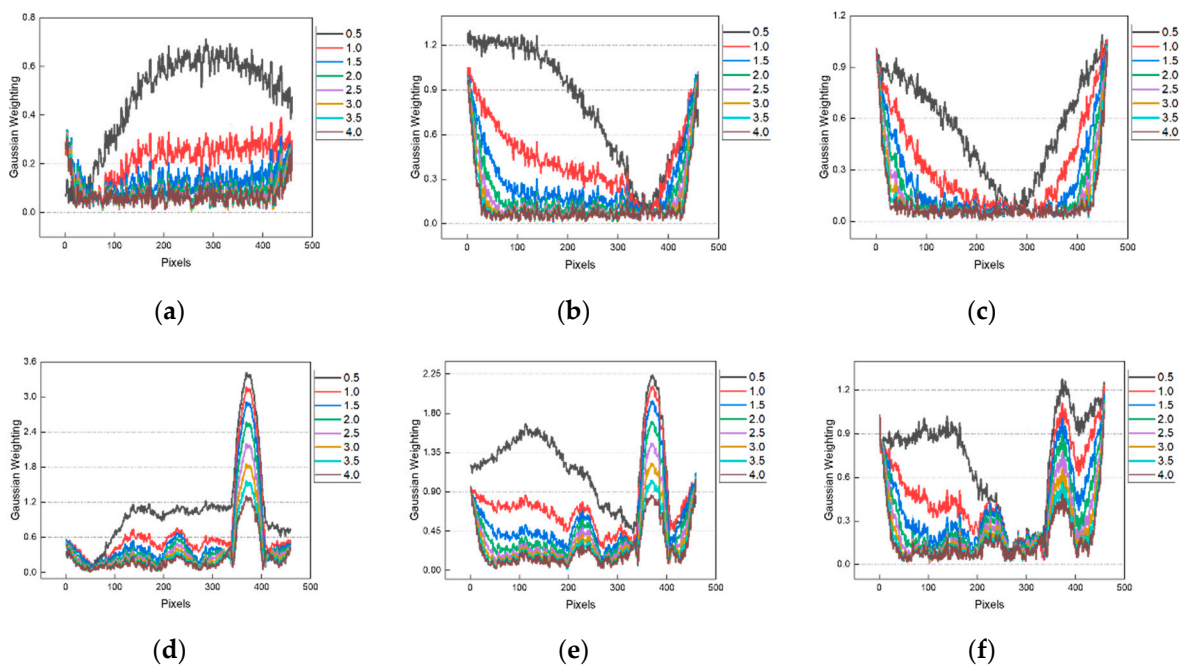


Figure 21. Amplitude profile graph of Line 2 to which FFT of B-type specimen was applied. (a) A-type, center; (b) A-type, left side; (c) A-type, top left; (d) B-type, center; (e) B-type, left side; (f) B-type, top left.

The detectability of thinning defects due to thermal equalization was evaluated by applying the FFT algorithm to the raw image, phase image, and amplitude image. In the case of the raw images, the thermal equalization had a significant impact but did not significantly contribute to detectability. In the case of the phase images, when the FFT algorithm was applied, noise occurred as the Gaussian weight increased, and detectability significantly decreased. In the case of the amplitude images, when the FFT algorithm was applied, the high-frequency components moved to the side, greatly increasing the detectability. However, as the Gaussian weight increases, the high-frequency data of the defective area decreases, and the detectability significantly decreases, so appropriate settings are required. Therefore, the SNR was evaluated to verify the validation of the FFT algorithm.

#### 4.4. Validation Evaluation of FFT algorithm

##### 4.4.1. Qualitative Evaluation Using Otsu Algorithm

When applying the FFT algorithm, the Otsu algorithm was used to verify its effectiveness. The Otsu algorithm is a technique that uses a grayscale-based histogram to calculate the optimal threshold for classifying light and dark values into 0 and 1. This algorithm is widely used to detect clear defects in the field of IRT. Figure 22 shows the binarization image using the Otsu algorithm in Figure 18. The distribution due to the excitation of the non-uniform heat source can be clearly confirmed in the binarization image. This causes difficulties in detecting thickness defects.

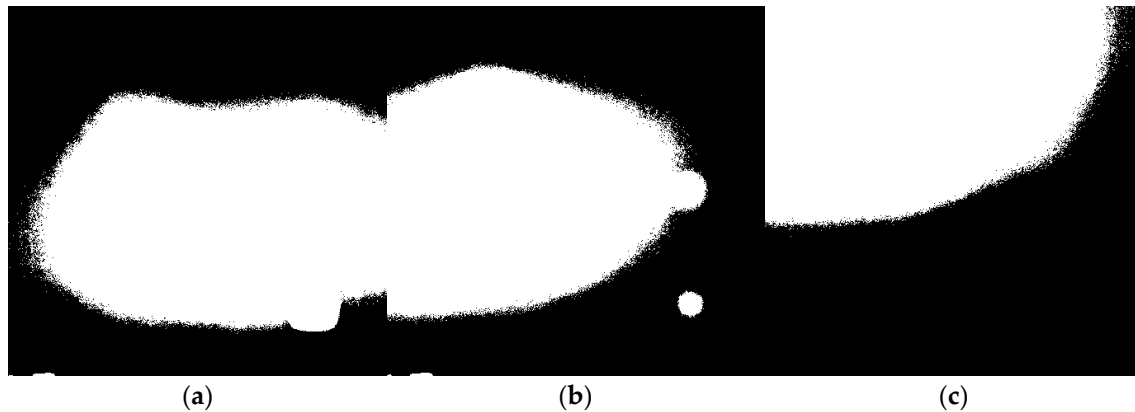


**Figure 22.** Binarization images of B-type specimen without FFT algorithm applied. (a) center; (b) left side; (c) top left.

Figure 23 shows the binarization image using the Otsu algorithm shown in Figure 20. Unlike in Figure 22, by applying the FFT algorithm, it can be seen that the image in which most of the heat sources have uneven distribution has been resolved. However, there is a distribution of high frequencies on the left and right sides, as seen in Figure 22b, and on all the edges, as seen in Figure 22c. Increasing the Gaussian weight reduces the influence of high frequencies, but it is also affected by defects, so setting an appropriate Gaussian weight is required.

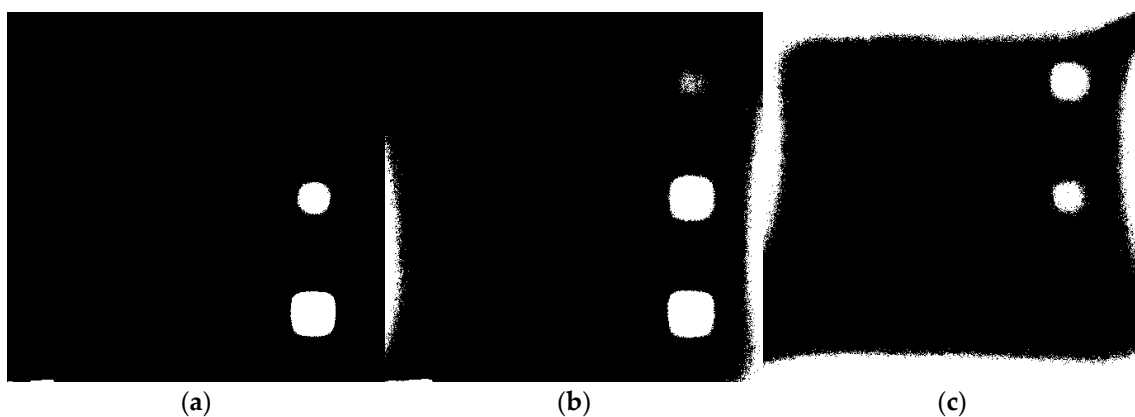


**Figure 23.** Binarization images of B-type specimen with FFT algorithm applied. (a) center; (b) left side; (c) top left.

##### 4.4.2. Quantitative Evaluation Using SNR

The SNR was evaluated to quantitatively verify the effectiveness of the FFT algorithm for the three types of heat sources. The SNR was calculated for thinning rates of 30, 50, 60,

70, 80, and 90% and was compared with the amplitude image without FFT applied. The formula for SNR is as follows [23]:

$$SNR = 20\log_{10}\left(\frac{|DROI_{mean} - SROI_{mean}|}{\sigma}\right) \tag{8}$$

where  $DROI_{mean}$  is the detective area,  $SROI_{mean}$  is the sound area, and  $\sigma$  is the standard deviation. Figures 24–26 show graphs evaluating the SNR depending on whether or not the FFT algorithm is applied. The red SNR value in the graph means the SNR value without the FFT algorithm is applied.

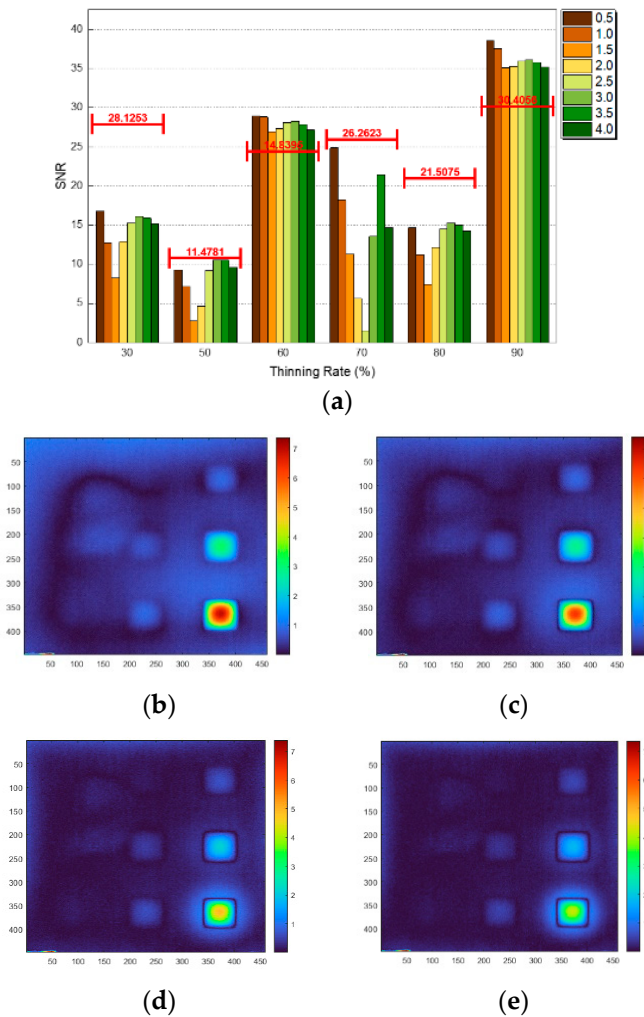


**Figure 24.** SNR graph of amplitude image based on FFT algorithm applying center thermal excitation. (a) center; (b) 1.0; (c) 1.5; (d) 2.5; (e) 3.0; (b–e) refer to Gaussian weights.

Figure 24a shows the effect of the FFT algorithm at thinning rates of 60 and 90%. At thinning rates of 30, 50, 70, and 90%, the SNR decreased when the FFT algorithm was applied. When looking at the trend of the SNR for all the thinning rates, a pattern in which the value of the Gaussian weight decreases and then increases can be seen. For this reason, as shown in Figure 24b,c, the value of the Gaussian weight is approximately 1.0 to 2.0, which is when the high-frequency component begins to move to the side. Additionally, Figure 24d,e show a trend in which the high-frequency component moves to the side and the SNR value increases. As the high-frequency component moves to the side, it overlaps with the defective area, and the SNR value decreases when calculating the defect area of the region of interest (ROI).

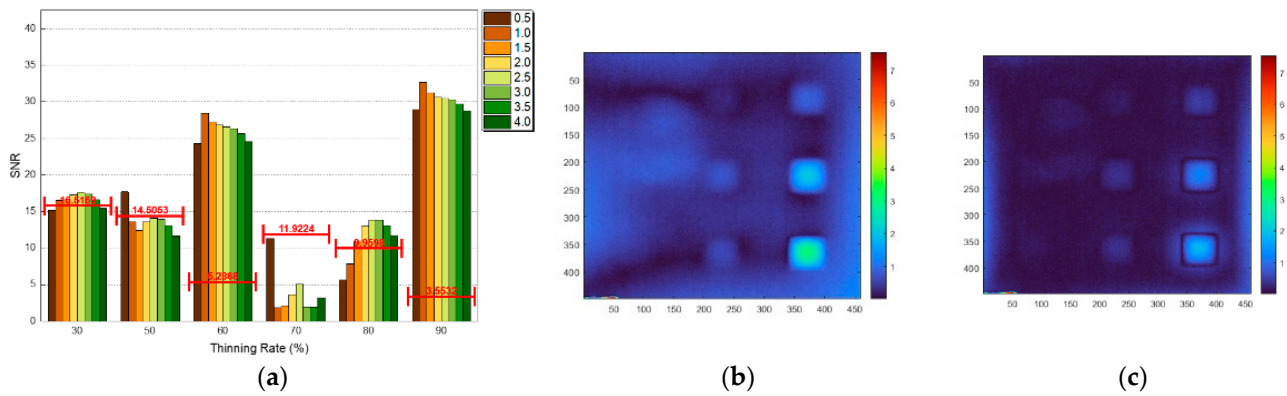


**Figure 25.** SNR graph of amplitude image based on FFT algorithm applying left side thermal excitation. (a) left side; (b) 1.0; (c) 3.0; (b,c) refer to Gaussian weights.

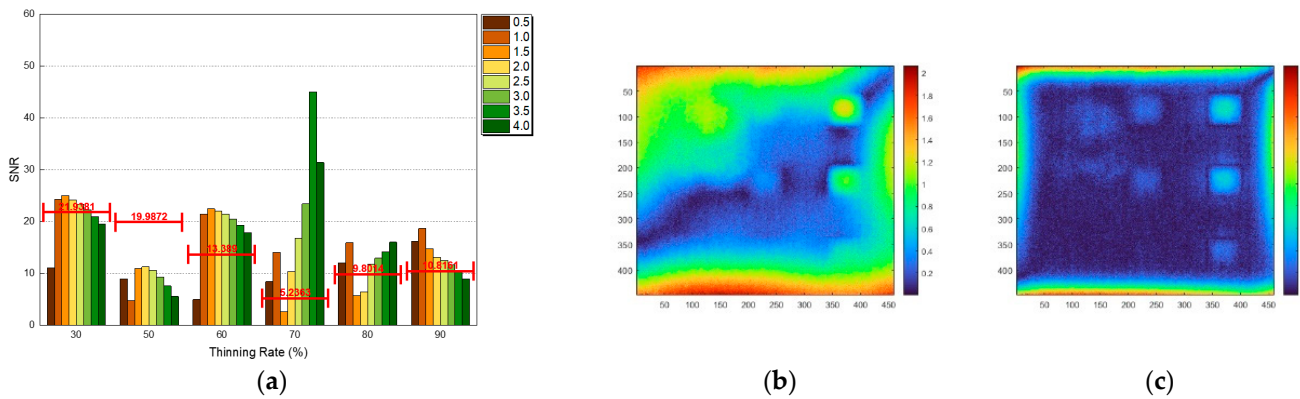


**Figure 26.** SNR graph of amplitude image based on FFT algorithm applying top left thermal excitation. (a) top left; (b) 1.0; (c) 3.0; (b,c) refer to Gaussian weights.

Figure 25a shows the effect of the FFT algorithm at all the thinning rates except for the 70% thinning rate. The SNR decreases when the FFT algorithm is applied at 70% because, as shown in Figure 25b, the high-frequency component overlaps with the area of the 70% thinning rate and is affected when calculating the SNR. Additionally, as seen in Figure 25c, the shape of the defect could not be confirmed, so the SNR was calculated to be close to 0.

Figure 26a shows the effect of the FFT algorithm at all the thinning rates except for the 50% thinning rate. As shown in Figure 18c, the amplitude image to which the FFT algorithm is not applied cannot confirm the shape of the defect, making the evaluation of the SNR meaningless. In particular, as shown in Figure 26b,c, when compared to the images with amplitudes at which the FFT algorithm was not applied, excellent effects can be seen at the thinning rates of 30, 60, and 90%, corresponding to column C.

When quantitatively evaluating the amplitude image and the SNR without the FFT algorithm applied, excellent effects can be confirmed in the form of heat excitation on the sides rather than at the center. However, when evaluating the SNR, the ROI location of the  $SROI_{mean}$  is very important, but since the normalization process for the image is impossible, clear validation is difficult. However, when analyzed qualitatively (visually), the effect can be clearly confirmed in the binarization image acquired using the Otsu algorithm. By applying the results of this study as basic data, it is expected to be used when inspecting large-area structures, including CLPs, in the future.

### 5. Conclusions and Future Research

This study conducted a study on thermal equalization of S275 specimens used in CLPs using the optical IRT technique. For thermal equalization, the Gaussian filtering-based

FFT algorithm was applied. The study used two types of heat sources, long pulse and sine wave, and three locations of the heat sources: center, left side, and top left.

First, thermal images were analyzed by exciting a long pulse heat source. When the FFT algorithm was applied to the thermal image of the A-type specimen, as the Gaussian weight increased, the effect of the thermal equalization increased. However, as the thermal equalization effect increased in the B-type specimen, the detectability decreased.

Second, the phase image of the LIT technique was analyzed by exciting a sine wave heat source. When the FFT algorithm was applied, a pattern occurred in which noise was concentrated in the center as the Gaussian weight increased. As a result, detection is possible due to the boundary line of the defective area, but when analyzing the graph, the contrast between the defective area and the sound area is not clear due to noise.

Third, the amplitude image of the LIT technique was analyzed by exciting a sine wave heat source. As the Gaussian weight increases, the high-frequency component moves to the side, creating a clear contrast between the defective area and the sound area. The effect of the FFT algorithm can be clearly seen in the binarized image acquired using the Otsu algorithm. Additionally, when comparing the SNR for the three heat source types, high performance can be seen on the left side and top left when an uneven heat source occurs on the side.

The noise present in thermal images can be effectively processed through Gaussian filtering, and at the same time, it is considered a very effective mechanism as it can resolve uneven thermal distribution. In addition, the thermal images acquired through the eddy current thermography (ECT) technique show localized heat concentration at the corners due to Joule's heating. Therefore, it can be expected that excellent effects will be obtained by applying the FFT algorithm presented in this study. Future research will perform super-resolution conversion using the very deep super-resolution (VDSR) deep neural network to remove noise and improve the blurring phenomenon caused by applying the FFT algorithm based on the data of this study.

**Author Contributions:** Conceptualization, S.L. and W.K.; methodology, Y.C.; software, S.L.; validation, S.L., Y.C. and H.S.; formal analysis, H.S.; investigation, S.L.; resources, Y.C.; data curation, S.L.; writing—original draft preparation, S.L.; writing—review and editing, W.K. and H.S.; visualization, Y.C.; supervision, W.K. and H.S.; project administration, W.K.; funding acquisition, W.K. All authors have read and agreed to the published version of the manuscript.

**Funding:** This work was supported by the Technology Development Program (S3249835) funded by the Ministry of SMEs and Startups (MSS, Korea).

**Institutional Review Board Statement:** Not applicable.

**Informed Consent Statement:** Not applicable.

**Data Availability Statement:** The data are only available upon reasonable request.

**Conflicts of Interest:** The authors declare no conflicts of interest.

## References

1. Yeom, Y.T.; Choi, Y.W.; Kim, H.J.; Kim, H.H.; Park, J.S.; Ryu, S.W.; Song, S.J. Containment Liner Plate Void Defect Detection Technique Using Phased Array Ultrasonic Testing and Acoustic Resonance Method. *Materials* **2022**, *15*, 1330. [[CrossRef](#)] [[PubMed](#)]
2. Dunn, D.S.; Pulvirenti, A.L.; Hiser, M.A. *Containment Liner Corrosion Operating Experience Summary*; US-NRC Report; U.S. Nuclear Regulatory Commission: North Bethesda, MD, USA, 2011; pp. 1–30.
3. Park, J.; Hong, J. Present status of nuclear containments and ISI in Korea. *Prog. Nucl. Energy* **2009**, *51*, 761–768. [[CrossRef](#)]
4. Kim, C.; Kang, S.; Chung, Y.; Kim, O.; Kim, W. Quantification of the Effective Detectable Period for Concrete Voids of CLP by Lock-In Thermography. *Appl. Sci.* **2023**, *13*, 8247. [[CrossRef](#)]
5. Hoła, J.; Bień, J.; Schabowicz, K. Non-destructive and semi-destructive diagnostics of concrete structures in assessment of their durability. *Bull. Pol. Acad. Sci. Tech. Sci.* **2015**, *63*, 87–96. [[CrossRef](#)]
6. Wiggenhauser, H. Advanced NDT methods for quality assurance of concrete. In Proceedings of the NDTCE'09, Non-Destructive Testing in Civil Engineering, Nantes, France, 30 June–3 July 2009.
7. Lee, Y.; Yun, H.; Cho, Y. Study of concrete de-bonding assessment technique for containment liner plates in nuclear power plants using ultrasonic guided wave approach. *Nucl. Eng. Technol.* **2022**, *54*, 1221–1229. [[CrossRef](#)]

8. Han, S.W.; Cho, S.H.; Kang, T.; Moon, S.I. Design and test of electromagnetic acoustic transducer applicable to wall-thinning inspection of containment liner plates. *Trans. Korean Soc. Press. Vessel. Pip.* **2019**, *15*, 46–52.
9. Mouritz, A.P.; Townsend, C.; Khan, M.S. Non-destructive detection of fatigue damage in thick composites by pulse-echo ultrasonics. *Compos. Sci. Technol.* **2000**, *60*, 23–32. [[CrossRef](#)]
10. Liang, M.T.; Su, P.J. Detection of the corrosion damage of rebar in concrete using impact-echo method. *Cem. Concr. Res.* **2001**, *31*, 1427–1436. [[CrossRef](#)]
11. Zhang, J.K.; Yan, W.; Cui, D.M. Concrete condition assessment using impact-echo method and extreme learning machines. *Sensors* **2016**, *16*, 447. [[CrossRef](#)]
12. Maldague, X.P. Introduction to NDT by Active Infrared Thermography. *Mater. Eval.* **2002**, *60*, 1060–1073.
13. Bagavathiappan, S.; Lahiri, B.B.; Saravanan, T.; Philip, J.; Jayakumar, T. Infrared thermography for condition monitoring—A review. *Infrared Phys. Technol.* **2013**, *60*, 35–55. [[CrossRef](#)]
14. Liu, Y.; Wang, F.; Liu, K.; Mostacci, M.; Yao, Y.; Sfarra, S. Deep convolutional autoencoder thermography for artwork defect detection. *Quant. InfraRed Thermogr. J.* **2023**, 1–17. [[CrossRef](#)]
15. Akhloufi, M.A.; Guyon, Y.; Castanedo, C.I.; Bendada, A. Three-dimensional thermography for non-destructive testing and evaluation. *Quant. InfraRed Thermogr. J.* **2017**, *14*, 79–106. [[CrossRef](#)]
16. Liu, K.; Zheng, M.; Liu, Y.; Yang, J.; Yao, Y. Deep autoencoder thermography for defect detection of carbon fiber composites. *IEEE Trans. Ind. Inform.* **2022**, *19*, 6429–6438. [[CrossRef](#)]
17. Wu, S.; Gao, B.; Yang, Y.; Zhu, Y.; Burrascano, P.; Laureti, S.; Rici, M.; Wang, Y. Halogen optical referred pulse-compression thermography for defect detection of CFRP. *Infrared Phys. Technol.* **2019**, *102*, 103006. [[CrossRef](#)]
18. Liu, T.; Zhang, W.; Yan, S. A novel image enhancement algorithm based on stationary wavelet transform for infrared thermography to the de-bonding defect in solid rocket motors. *Mech. Syst. Signal Process.* **2015**, *62*, 366–380. [[CrossRef](#)]
19. Łukaszuk, R.D.; Marques, R.M.; Chady, T. Lock-In Thermography with Cooling for the Inspection of Composite Materials. *Materials* **2023**, *16*, 6924. [[CrossRef](#)] [[PubMed](#)]
20. D’Accardi, E.; Palumbo, D.; Galietti, U. A comparison among different ways to investigate composite materials with lock-in thermography: The multi-frequency approach. *Materials* **2021**, *14*, 2525. [[CrossRef](#)] [[PubMed](#)]
21. Matarrese, T.; Palumbo, D.; Galietti, U. Comparison in the transient regime of four lock-in thermography algorithms by means of synthetic and experimental data on CFRP. *NDT E Int.* **2023**, *139*, 102925. [[CrossRef](#)]
22. Lee, S.; Chung, Y.; Kim, C.; Shrestha, R.; Kim, W. Thermographic inspection of CLP defects on the subsurface based on binary image. *Int. J. Precis. Eng. Manuf.* **2022**, *23*, 269–279. [[CrossRef](#)]
23. Chung, Y.; Shrestha, R.; Lee, S.; Kim, W. Thermographic inspection of internal defects in steel structures: Analysis of signal processing techniques in pulsed thermography. *Sensors* **2020**, *20*, 6015. [[CrossRef](#)] [[PubMed](#)]

**Disclaimer/Publisher’s Note:** The statements, opinions and data contained in all publications are solely those of the individual author(s) and contributor(s) and not of MDPI and/or the editor(s). MDPI and/or the editor(s) disclaim responsibility for any injury to people or property resulting from any ideas, methods, instructions or products referred to in the content.